RSC Advances

ROYAL SOCIETY OF CHEMISTRY

www.rsc.org/advances

TOC Graphic

The presence of oxygen vacancies and synergetic interaction between Ce and Mn were responsible for superior Hg^0 oxidation performance of CeO_2–MnO_x compared to pure CeO_2 and MnO_x

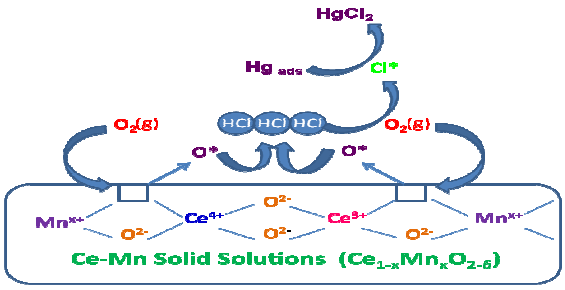

Cite this: DOI: 10.1039/c0xx00000x

www.rsc.org/xxxxxx

ARTICLE TYPE

Catalytic oxidation and adsorption of elemental mercury over nanostructured CeO_2–MnO_x catalyst

Deshetti Jampaiah[a,b], Katie M. Tur[b], Perala Venkataswamy[a], Samuel J. Ippolito[b], Ylias M. Sabri[b], James Tardio[b], Suresh K. Bhargava*[b] and Benjaram M. Reddy*[a]

Received (in XXX, XXX) Xth XXXXXXXXX 20XX, Accepted Xth XXXXXXXXX 20XX
DOI: 10.1039/b000000x

Abstract A nanostructured CeO_2–MnO_x catalyst was synthesized by coprecipitation method and subjected to different calcination temperatures at 773 and 1073 K to understand the surface structure and the thermal stability. The structural and redox properties were deeply investigated by various techniques, namely, X-ray diffraction (XRD), inductively coupled plasma-optical emission spectroscopy (ICP-OES), Brunauer–Emmett–Teller (BET) surface area, transmission electron microscopy (TEM), Raman spectroscopy (RS), hydrogen-temperature programmed reduction (H_2-TPR), and X-ray photoelectron spectroscopy (XPS). The CeO_2–MnO_x catalyst calcined at 773 K was tested towards elemental mercury (Hg^0) oxidation and the achieved results are compared with the pure CeO_2 and MnO_x. The XRD and TEM results confirmed the incorporation of Mn ions into the ceria lattice and the formation of nanostructured solid solution, respectively. The RS and TPR results showed that CeO_2–MnO_x catalyst exhibits more oxygen vacancies with superior redox ability over CeO_2 and MnO_x. XPS analysis indicates that Ce and Mn existed in multiple oxidation states. Compared to pure CeO_2 and MnO_x, the CeO_2–MnO_x catalyst exhibited more Hg^0 oxidation efficiency (E_{oxi}) of 11.7, 33.5, and 89.6% in the presence of HCl, O_2, and HCl/O_2-mix conditions, respectively. The results clearly indicated that the HCl/O_2-mix had a promotional effect on the catalytic Hg^0 oxidation. This was most likely due to the presence of surface oxygen species and oxygen vacancies being generated by a synergetic effect between CeO_2 and MnO_x. In the presence of HCl, the CeO_2–MnO_x catalyst exhibited good adsorption efficiency (E_{ads}) of 92.4% over pure CeO_2 (46.5%) and MnO_x (80.6%). It was found that by increasing the operating temperature from 423 to 573 K resulted in considerable increase of E_{oxi} and a decrease in the sorption of Hg^0 on the catalyst.

1. Introduction

The emission of mercury (Hg) from anthropogenic sources is becoming a serious global concern that attracts considerable attention in recent years. Mercury is a volatile and persistent pollutant that accumulates in the food chain and has a serious neurological health effects in humans.[1,2] Among various emission sources, the coal-fired power plants account for 24% of global anthropogenic Hg emissions and they are considered as the major emission source partly due to their unintentional Hg emissions during heating and power generation activities.[3] In recent decades, many countries, especially in the developed countries, have taken steps to reduce Hg emissions. Generally, in a coal derived flue gas, there are three forms of Hg, namely, elemental mercury (Hg^0), oxidized mercury (Hg^{2+}), and mercury associated with particulate matter (Hg_P).[4] Unlike Hg^{2+} and Hg_p, Hg^0 is difficult to remove using wet flue gas desulfurization (FGD) units and electrostatic precipitators (ESP) due to its high volatility and low solubility in water.[5,6] A variety of technologies have been investigated to constrain Hg^0 from the flue gas. Among them, the current state of the art technology for controlling Hg^0 emissions is Activated Carbon Injection (ACI).[7–9] However, this technology has a few drawbacks such as high operation expenses, poor capacity, narrow temperature range of application, and slow adsorption and regeneration rates.[10] In order to overcome these concerns, the catalytic oxidation of Hg^0 to Hg^{2+} could be a promising approach for controlling anthropogenic Hg^0 emissions from coal-fired power plants in a cost effective and environmentally friendly manner.[11]

It is well-known that coal-fired power plants emit Hg^0 into the environment during the combustion processes that occur at high temperatures (up to 1700 K). Subsequently, homogeneous oxidation can take place during the post combustion phase when temperatures drop to ranging from approximately 750 to 900 K allowing the formation of $HgCl_2$. Similarly there is a possibility of formation of oxidized Hg species (e.g. $HgCl_2$ or HgO) by heterogeneous catalytic oxidation as the stack gas temperature drops to 398–598 K. Accordingly, Hg^0 vapor is known to mostly react with Cl_2, HCl, and O_2 in the stack gas, and undergo reactions to a lower extent with other species (e.g. NH_3, N_2O and

[a]RMIT-IICT Joint Research Centre, CSIR-Indian Institute of Chemical Technology, Uppal Road, Hyderabad – 500 007, India E–mail addresses: bmreddy@iict.res.in; mreddyb@yahoo.com Phone: +91 40 2719 3510; fax: +91 40 2716 0921.
[b]Centre for Advanced Materials & Industrial Chemistry (CAMIC), School of Applied Sciences, RMIT University, GPO BOX 2476, Melbourne–3001, Australia. E-mail: suresh.bhargava@rmit.edu.in; Tel: +61 3 9925 3365

H_2S).[12,13] For the oxidization of elemental mercury by chlorine and oxygen, there is also a correlation between HCl concentration in the flue gas and the extent of elemental mercury oxidised.[14] These facts show that the occurrence of Hg^0 oxidation largely relies on the presence of oxidants such as HCl and O_2. So, catalytic oxidation of Hg^0 using gaseous O_2 and HCl in the flue gas as the oxidants is a simple and economical method for Hg^0 control. However, the major challenge is the selection of the proper catalysts for this purpose. In recent years, transition metal oxides appear to be promising candidates due to their much lower cost, high catalytic activity towards catalytic oxidation reactions and temperature stability relative to noble metal based catalysts.[15] Several metal oxides such as CuO, Cu_2O, MnO_x, Fe_2O_3, TiO_2, VO_x/TiO_2, and Co/TiO_2 have already been investigated for the catalytic Hg^0 oxidation reaction ($Hg^0 \rightarrow Hg^{2+}$).[16–18] These studies have demonstrated the feasibility of using metal oxides to catalyze the oxidation of Hg^0 in the presence of hydrochloric acid (HCl) according to the following reaction:

$$Hg^0 + 2HCl + ½\ O_2 \rightarrow HgCl_2 + H_2O \quad (1)$$

Among the various investigated metal oxide catalysts, manganese oxides have been studied extensively for several catalytic oxidation reactions such as partial or total oxidation of hydrocarbons due to its ability to exist in multiple oxidation states.[19] In terms of catalyst efficiency, it is well reported that the Hg^0 oxidation efficiency over MnO_x/alumina and modified MnO_x/alumina catalysts can reach more than 90%, and Mn^{4+} species are the most active components among the various manganese valence states.[20] Ji *et al.*[21] also reported that MnO_x/TiO_2 catalyst is effective for Hg^0 oxidation with high capacity (17.4 mg Hg^0 g^{-1} catalyst) at elevated temperatures of 448–473 K. The observed elemental mercury capacities were much higher than the capacities of commercially available activated carbons. They believed that Hg^0 oxidation over Mn-based catalysts could be explained by Mars-Massen mechanism because HgO was found in the spent catalyst and lattice oxygen participated during the reaction. In other words, surface oxygen including lattice oxygen, chemisorbed or weakly bonded oxygen are very important for Hg^0 oxidation over MnO_x based catalysts.[22] Although, MnO_x materials showed excellent catalytic performance for Hg^0 conversion at higher temperatures, they were less active at low temperatures with the presence of SO_2 adding a significantly negative effect on Hg^0 conversion.[23,24] Therefore, a combination of MnO_x and a material with a large oxygen storage capacity (OSC) is thought to facilitate Hg^0 oxidation at lower temperatures around 423 K. An example is the CeO_2 catalyst which has been extensively studied for various catalytic processes due to its high OSC as a result of its property of storing and releasing O_2 via the Ce^{4+}/Ce^{3+} redox couple.[25] The success of CeO_2 stems from the easy generation of oxygen vacancies that facilitate activation and transport of oxygen species. The generated surface oxygen vacancies and bulk oxygen species with relatively high mobility are very active for oxidation processes.[5] Recently, various supports such as modified pillared clays (PILCs)-, titania (TiO_2)-, and alumina (Al_2O_3)- supported CeO_2–MnO_x mixed oxides were studied for Hg^0 oxidation.[20,25,26] It was found that the synergy between CeO_2 and MnO_x as well as facile oxygen mobility were responsible for superior Hg^0 oxidation performance. To the authors' knowledge, the unsupported CeO_2–MnO_x mixed oxide for mercury oxidation rarely reported in the literature. Hence, the major objective of the present study was to investigate Hg^0 oxidation and adsorption efficiencies using CeO_2–MnO_x as the catalyst under different industrial flue gas conditions.

2. Experimental

2.1. Catalyst preparation

The CeO_2–MnO_x (Ce/Mn 7:3 mole ratio based on oxides) catalyst was prepared by a coprecipitation method using $Ce(NO_3)_3.6H_2O$ (Aldrich, AR grade) and $Mn(NO_3)_2.4H_2O$ (Merck, AR grade) precursors. In a typical procedure, requisite quantities of precursors were dissolved separately in deionized water and mixed together. After, the aqueous NH_3 was added drop-wise with vigorous stirring until the precipitation was complete (pH ~9). The resulting product was filtered off, washed several times with deionized water, and oven dried at 383 K for 12 h. Finally, the catalyst was calcined at 773 K for 5 h in air atmosphere and denoted as CeMnO-773. In order to investigate the thermal stability of the catalyst, some portions of the catalyst was once again heated at 1073 K for 5 h and the final catalyst was designated as CeMnO-1073. For comparison, pure ceria (CeO_2) and manganese oxide (MnO_x) were also prepared by the same precipitation method.

2.2. Catalyst characterization

The X-ray diffraction measurements were performed on a Rigaku Multiflex diffractometer equipped with a nickel-filtered Cu-Kα (1.5418 Å) radiation source and a scintillation counter detector. The diffraction patterns were recorded over a 2θ range of 10–80° with a 0.021 step size and using a counting time of 1 s per point. The XRD phases present in the samples were identified with the help of the Powder Diffraction File from the International Centre for Diffraction Data (PDF-ICDD). The mean crystallite size (D) was measured by applying the Scherrer equation. The cell parameters (*a*) of various catalysts were calculated by a standard cubic indexation method using the intensity of the base peak (111). The chemical analysis of the prepared samples was performed using inductively coupled plasma-optical emission spectroscopy (ICP-OES, Thermo Jarrel Ash model IRIS Intrepid II XDL, USA) to confirm the respective concentrations of elements in the system. For ICP analysis, approximately 50 mg of the sample was dissolved in a solution of 25 mL aqua regia and 475 mL distilled water. Then 10 mL of the above solution was diluted to 250 mL.

The surface areas and pore size distribution of the as-prepared samples were determined by N_2 adsorption-desorption isotherms at liquid N_2 temperature (77 K) on a Micromeritics (ASAP 2000) analyzer. Specific surface area and pore size distribution were calculated by Brunauer-Emmett-Teller (BET) and Barrett-Joyner-Halenda (BJH) methods, respectively. Prior to analysis, the samples were degassed at 393 K for 2 h to remove the surface adsorbed residual moisture.

Transmission electron microscopy (TEM) studies were carried out on a JEM-2010 (JEOL) instrument equipped with a slow-scan CCD camera and at an accelerating voltage of 200 kV. Samples for TEM analysis were prepared by crushing the materials in an agate mortar and dispersing them ultrasonically in ethyl alcohol. Afterward, a drop of the dilute suspension was placed on a perforated-carbon-coated copper grid and allowed to dry by evaporation at ambient temperature.

Raman spectra were collected on a DILORXY spectrometer equipped with a liquid nitrogen-cooled CCD detector. The samples were excited with the emission line at 632 nm from an Ar^+ ion laser (Spectra Physics), which was focused on the sample under the microscope with the diameter of the analyzed spot being ~1 μm. The acquisition time was adjusted according to the intensity of the Raman scattering. The wavenumber values obtained from the spectra were precise to within 2 cm^{-1}.

The reducibility of the catalysts was studied by H_2-TPR analysis using a thermal conductivity detector of a gas chromatograph (Shimadzu). Prior to the reduction, approximately 30 mg of the sample was loaded in an isothermal zone of the reactor and pre-treated in a helium gas flow at 473 K and then cooled to room temperature. Then, the sample was heated at a rate of 10 K min^{-1} from ambient temperature to 1100 K in a 20 mL min^{-1} flow of 5% H_2 in Ar. The hydrogen consumption during the reduction process was estimated by passing the effluent gas through a molecular sieve trap to remove the produced water and it was analyzed by gas chromatography using the thermal conductivity detector.

The XPS measurements were performed on a Shimadzu ESCA 3400 spectrometer using Mg-Kα (1253.6 eV) radiation as the excitation source at room temperature. The samples were maintained in a strict vacuum typically on the order of less than 10^{-8} Pa to avoid a large amount of noise in the spectra from contaminants. The obtained binding energies were corrected by referencing the spectra to the carbon (C 1s) peak at 284.6 eV.

2.3. Catalyst activity studies

The catalytic oxidation of Hg^0 was evaluated using a bench-scale experimental system as shown in Fig. S1 (ESI†). The apparatus consisted of several components including a temperature-controlled quartz reactor, mercury speciation trapping system, HCl vapour and Hg^0 vapor generators. The Hg^0 oxidation tests were performed with the total gas flow rate set at 0.2 L min^{-1}. A mercury permeation device (VICI, Metronics Inc.) was used as the source of Hg^0 (~320 μg m^{-3}). The N_2 was used as the carrier gas to transport Hg^0 vapor out of the permeation tube holder. All the individual flue gases were precisely controlled by mass flow controllers. The typical composition of a simulated flue gas (SFG) mixture was 3% O_2, 5% CO_2, 10 ppm HCl, and balanced with dry N_2. The reactor was loaded with a small portion of quartz wool to support the catalyst layer and avoid its loss. In each test, 0.4 g of catalyst was loaded into the isothermal zone of the reactor. The reactor system was gradually heated under N_2 gas to reach the desired temperature (423 K). During the experiment, the catalyst was exposed to simulated flue gas for 16 h. The outlet gas stream was passed through a series of seven impingers to capture and speciate the outlet mercury. In this work, the arrangement of the traps was based on a variant of the Ontario Hydro Method (OHM),[27] in which the flue gas is passed through an absorbing media (KCl and $KMnO_4$ solutions). Then, the samples of the absorbing media are quantitatively analyzed for their Hg contents using an analytical instrument such as Agilent 7700 Series inductively coupled plasma mass spectrometer (ICP-MS). The KCl impinger solutions were employed to capture the Hg^{2+}, whereas $KMnO_4$ containing impinger solutions were used to capture the non-oxidised portion (i.e. elemental mercury). According to OHM, the oxidised mercury is calculated as the sum of mercury measured in the KCl impinger solutions, while the elemental mercury is the sum of the mercury measured in the $KMnO_4$ impinger solutions. The adsorbed mercury was then determined by digesting the spent catalyst. In this procedure, a known amount of sample was combined with 1 mL of aqua regia and one drop of $KMnO_4$ and then aged for overnight at room temperature. The purpose of the $KMnO_4$ in the digest media was to absorb any Hg^0 evolved in the closed container due to the heat released during the digestion process. Thus the digestion process dissolves all the adsorbed mercury into the supernatant, allowing the total amount of mercury to be determined using ICP-MS analysis. To establish a baseline prior to conducting the catalysis experiment, the total inlet mercury (Hg^0_{inlet}) was determined by performing a calibration experiment without the presence of any catalyst in the system. Based on this data, the Hg^0 oxidation efficiency (E_{oxi}) and the Hg^0 adsorption efficiency (E_{ads}) of the developed catalysts were determined by using the following equations:

$$E_{oxi} = \frac{Hg^{2+}}{Hg^0_{inlet}} \quad X\ 100\% \qquad (2)$$

$$E_{ads} = \frac{Hg_{ads}}{Hg^0_{inlet}} \quad X\ 100\% \qquad (3)$$

3. Results and discussion

3.1. Characterization studies

Fig. 1 illustrates the XRD patterns of MnO_x, CeO_2, and CeO_2–MnO_x mixed oxides calcined at different temperatures. The XRD pattern of MnO_x calcined at 773 K represents the Mn_2O_3 phase, which is well matched with the cubic Mn_2O_3 (JCPDS card no. 01-1061).[28] On the other hand, the CeO_2–MnO_x catalyst calcined at 773 K exhibits the characteristic peaks related to the fluorite structured CeO_2 (PDF-ICDD 34-0394).[29] The absence of Mn-oxide phases (MnO_2, Mn_2O_3, MnO, and Mn_3O_4) has been attributed to either the dispersion of MnO_x phases in ceria lattice or the Mn cations may be substituted instead of some Ce sites in the fluorite structure. Surprisingly, the CeO_2–MnOx catalyst calcined at 1073 K showed very weak Mn_2O_3 peaks along with CeO_2 peaks, which might be due to Mn-oxide phase segregation at elevated thermal treatments.[29] Further, an increase in the

Table 1 The surface areas (SA), pore volume (cm^3g^{-1}), pore size (nm), crystallite size (nm), and lattice parameter (Å) of CeO_2 and MnO_x catalysts calcined at 773 K, and CeO_2–MnO_x catalysts calcined at 773 and 1073 K.

Catalyst	Surface area (m^2g^{-1})	Pore volume (cm^3g^{-1})	Pore size (nm)	Crystallite size (nm)	Lattice parameter (Å)
CeO_2	39	0.11	9.8	8.9	5.41
MnO_x	8	0.02	12.3	32.4	4.71
CeMnO-773	58	0.44	6.2	7.2	5.35
CeMnO-1073	11	0.18	7.7	22.4	5.41

intensity and decrease in the peak width were observed in the XRD patterns at higher calcination temperatures. This may be due to the growing degree of the crystallinity of the samples.[30] The crystallite sizes were determined by using Scherrer equation for the CeO_2 (111) plane, the results of which are listed in Table 1. The CeMnO-773 catalyst exhibited a lower crystallite size (7.2 nm) compared to pure CeO_2 (8.9 nm). With increase in calcination temperature, the average crystallite size increased to 22.4 nm, which could be rationalized as a result of sintering.[31] Additionally, it was observed that the diffraction peaks of CeO_2–MnO_x catalysts were shifted slightly to higher angles compared to CeO_2, resulting from lattice contraction due to the substitution of Ce^{4+} by Mn^{x+} in the fluorite structure.[25] Because of this, the cell parameter of ceria (5.41 Å) decreases to 5.35 Å upon Mn doping (CeMnO-773 catalyst). These results imply that some manganese ions were incorporated into the ceria lattice, leading to the formation of a solid solution between manganese and cerium oxides. This observation is in agreement with Vegard's law, which holds that a linear relationship exists, at a constant temperature. As the calcination temperature increased to 1073 K, we observed a small increase in lattice parameter. Overall, these results confirm that the strong Ce–Mn–O interaction in the solid solution have effectively inhibited the crystalline growth and in turn improved the thermal stability of CeO_2–MnO_x catalyst.

Furthermore, the molar ratios of Ce/Mn in the CeO_2–MnO_x mixed oxides were determined by ICP-OES analysis, and the chemical compositions of the samples are shown in Table S1 (ESI†). The reported chemical compositions of the prepared samples were close to those of the initial mixed solutions.

Fig. 2 shows the profiles of adsorption-desorption curves of nitrogen isotherms for all the catalysts. The values of specific surface area, pore volume, and pore diameter of all catalysts are summarized in Table 1. The nanostructured CeMnO-773 catalyst exhibited a high BET surface area (58 m^2 g^{-1}) compared to pure CeO_2 and MnO_x. The high specific surface area of CeMnO-773 sample is probably due to the presence of smaller sized CeO_2 crystallites. However, as the calcination temperature increases to 1073 K, the surface area decreased to 11 m^2 g^{-1}. The decline of the surface area with increasing calcination temperature could be due to the increase in the particle size with temperature. Additionally, the CeO_2–MnO_x catalyst calcined at 773 K exhibited lower average pore diameter value, while compared to pure CeO_2 and MnO_x. However, the average pore size increased with increasing calcination temperature due to the larger size of the CeO_2 crystallites.

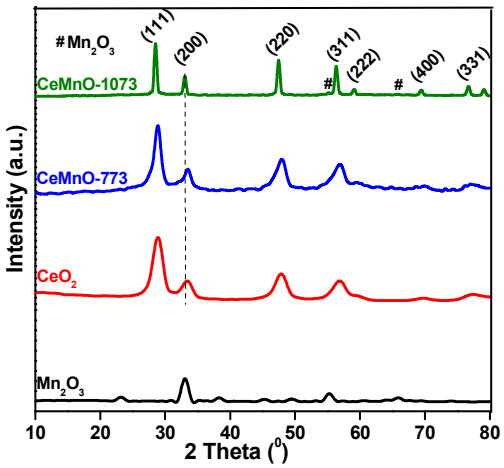

Fig. 1 Powder XRD patterns of MnO_x and CeO_2 catalysts calcined at 773 K, and CeO_2–MnO_x catalysts calcined at 773 and 1073 K.

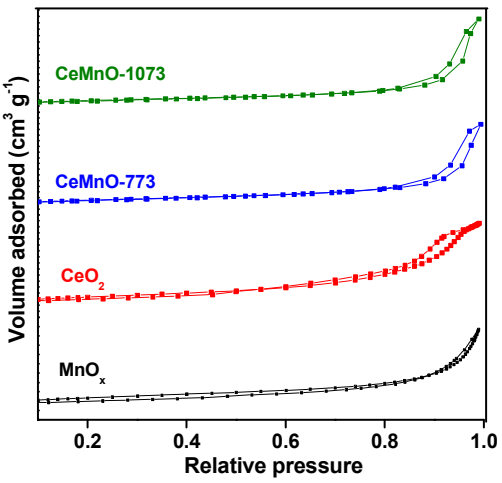

Fig. 2 Nitrogen adsorption-desorption isotherms MnO_x and CeO_2 catalysts calcined at 773 K, and CeO_2–MnO_x catalysts calcined at 773 and 1073 K.

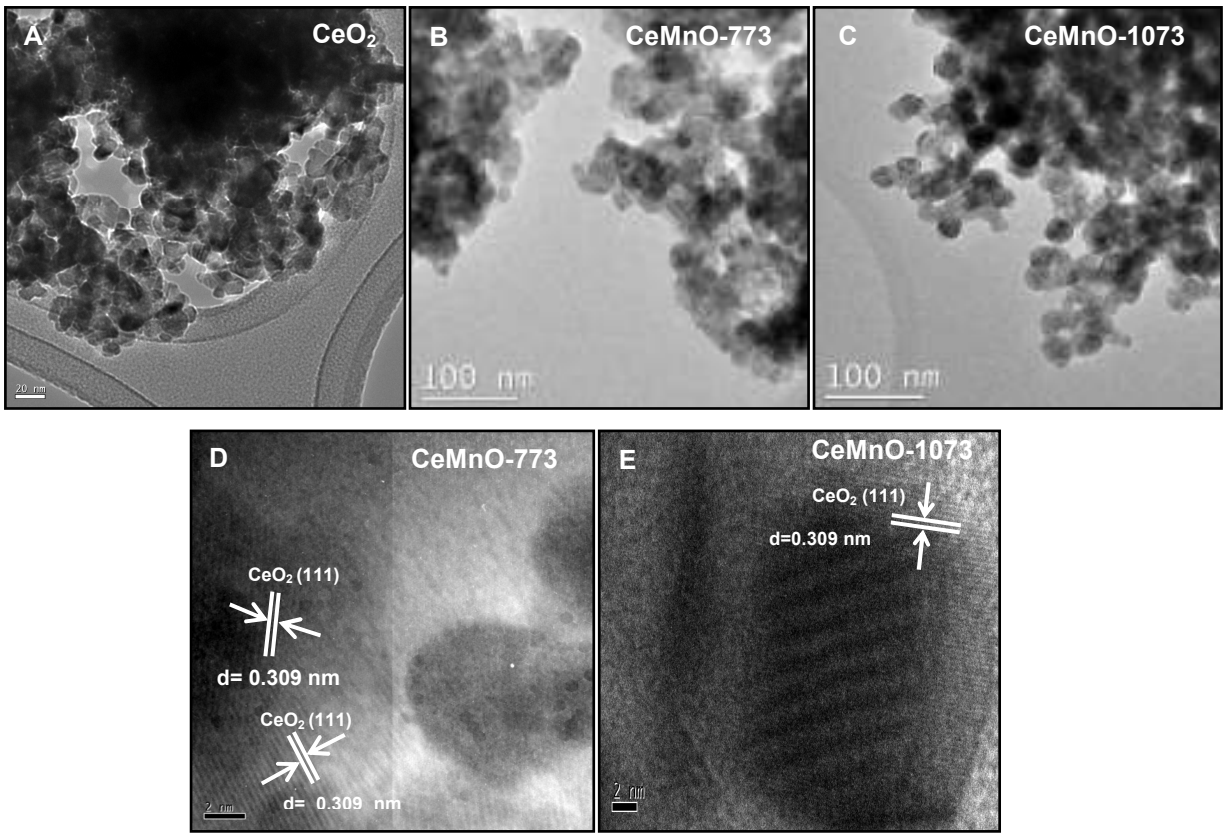

Fig. 3 TEM and HRTEM images of CeO_2 calcined at 773 K (A), CeO_2–MnO_x catalysts calcined at 773 K (B,D) and 1073 K (C,E).

The morphology and crystalline growth of samples were examined by TEM and HRTEM analyses and corresponding images are shown in Fig. 3. The nanosized and well dispersed particles (~7−20 nm) can be clearly observed for both CeO_2–MnO_x catalysts calcined at different temperatures (Fig. 3B and Fig. 3C). The average particle size of CeMnO-773 catalyst was ~7 nm, in reasonable agreement with the size calculated using the Scherrer equation (Table 1). The HRTEM images of CeMnO-773 and CeMnO-1073 samples (Fig. 3D and Fig. 3E) display the crystalline nature of the developed nanoparticles. The lattice fringes are clearly visible and planes with d_{111} spacing of 0.309 nm related to fluorite structured CeO_2 were observed in both samples. It clearly indicates the thermal stability of the CeO_2–MnO_x catalyst.[32,33]

Fig. 4 illustrates the Raman spectra of CeO_2–MnO_x catalysts along with pure CeO_2 and MnO_x. The Raman band at ~465 cm^{-1} for CeO_2 is related to the vibrational mode (F_{2g}) of fluorite-type structure, which can be regarded as a symmetric breathing mode of the oxygen ions around each Ce^{4+} cation.[34] On the other hand, the Raman spectra of CeMnO-773 and CeMnO-1073 catalysts displayed peaks at ~453 and ~459 cm^{-1}, respectively. This red shift of F_{2g} mode indicates the formation of solid solution between Ce and Mn that could deform the fluorite structure and form oxygen vacancies in the CeO_2 lattice. The presence of oxygen vacancies can be confirmed by the Raman mode at ~646 cm^{-1} for CeMnO-773 catalyst.[35] However, for CeMnO-1073 catalyst, the peaks at ~317, 363, and 653.9 cm^{-1} can be ascribed to the different phases such as Mn_3O_4 and Mn_2O_3.[36] In particular, Mn_2O_3 phase was detected by the XRD analysis indicating that Mn_2O_3 was segregated from the mixed oxide at elevated temperatures, which is strongly supported by XRD results. Based on these results, it can be stated that when a Ce^{4+} ion is substituted with a manganese ion, an oxygen vacancy is formed to maintain the charge balance, which plays an important role for Hg^0 oxidation.

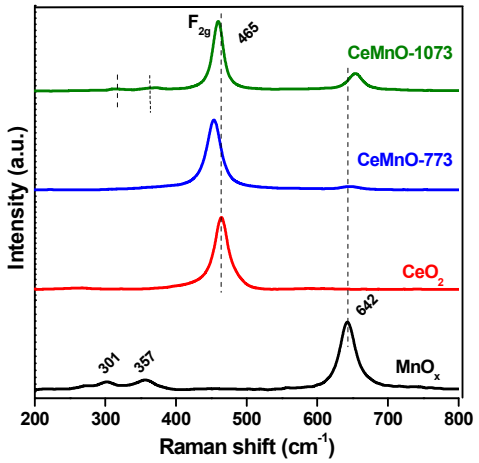

Fig. 4 Raman spectra of MnO_x and CeO_2 catalysts calcined at 773 K, and CeO_2–MnO_x catalysts calcined at 773 and 1073 K.

Table 2 Summary of binding energies of fresh catalysts collected from XPS.

Catalyst	Binding energies (eV)						
	Ce $3d_{3/2}$ (u‴)	Mn $2p_{3/2}$			O 1s		
		Mn^{4+}	Mn^{3+}	Mn^{2+}	O_I	O_{II}	O_{III}
MnO_x	-	643.9	641.6	640.4	529.3	531.3	-
CeO_2	916.4	-	-	-	530.2	531.9	-
CeMnO-773	915.3	643.2	641.2	640.1	529.1	530.5	532.7
CeMnO-1073	916.1	643.7	641.5	640.2	529.8	530.6	533.8

Fig. 5 shows the H_2-TPR profiles of CeO_2–MnO_x catalysts along with pure CeO_2 and MnO_x. Generally, pure ceria exhibits two reduction peaks corresponding to the surface and bulk reduction which are centred at ~793 and 1100 K (not shown), respectively.[37] The pure MnO_x also exhibited two reduction peaks at ~603 and 745 K. The first reduction peak at ~603 K can be ascribed to the reduction of MnO_2 and/or Mn_2O_3 to Mn_3O_4 while the second peak at ~745 K is generated because of the reduction of Mn_3O_4 to MnO.[38] As shown from Fig. 5, the reduction peaks of the CeO_2–MnO_x catalysts were observed at lower temperatures than those observed for both pure CeO_2 and MnO_x. It can be concluded that the reduction peak at a low temperature corresponds to the reduction of manganese oxide species (MnO_2 and/or Mn_2O_3), while the high temperature reduction peak could be attributed to the combined reductions of Mn_3O_4 and surface Ce-oxide species. The possible reason for this behavior is the enhancement of oxygen vacancies through the formation of solid solution, thereby increasing the lattice oxygen mobility and facilitating the diffusion of lattice oxygen from the bulk to the surface (as evidenced from Raman results).[31,39] Besides, as the calcination temperature increased, the reduction peaks were observed to shift to a higher temperature compared to CeMnO-773. This may be due to the slight segregation of Mn-oxide from CeO_2 lattice, which was supported by XRD and Raman results. However, the CeMnO-1073 catalyst showed prominent redox ability while compared to pure CeO_2 and MnO_x, indicating that the CeO_2–MnO_x catalyst was thermally stable. These results render that there may have formed a synergetic interaction between Ce and Mn that will possibly be useful for reactions such as the catalytic Hg^0 oxidation reaction.

Fig. 6A illustrates Ce 3d XP spectra of CeO_2, CeMnO-773, and CeMnO-1073 samples. The main features are composed of eight peaks labelled as u and v. The peaks labelled as u are due to $3d_{3/2}$ spin–orbit states, and those labelled as v are due to the corresponding $3d_{5/2}$ states. As can be noted from Fig. 6A, the six peaks labelled as u, u″, u‴, v, v″, v‴ are featured to Ce^{4+} ions, and the other 2 peaks labelled as u′ and v′ are related to Ce^{3+} ions.[40,41] From Table 2, it can be concluded that CeO_2–MnO_x samples exhibited the binding energy (u‴) lower than pure ceria, indicating that the doping influences the chemical environment of ceria. It is reported that the existence of Ce^{3+} in CeO_2 implies the formation of an oxygen vacancies.[42] As can be noted from Table 3, it is clear that Ce^{4+} and Ce^{3+} coexist in the sample, however the ratio of Ce^{4+} to Ce^{3+} changes. After Mn doping into CeO_2 lattice, the ratio decreased from 5.04 to 3.14, which indicates that reduced species Ce^{3+}, together with Mn^{3+} played a vital role in creating charge imbalance, vacancies, and unsaturated chemical bonds on the catalyst surface.[25] Therefore, the coexistence of Ce^{4+} and Ce^{3+} species at the surface could lead to the appearance of more oxygen vacancies in CeO_2–MnO_x catalyst, which is in agreement with the Raman analysis. Based on the observed phenomena, it can be concluded that the combination of CeO_2 and MnO_x could facilitate more surface oxygen for Hg^0 oxidation.

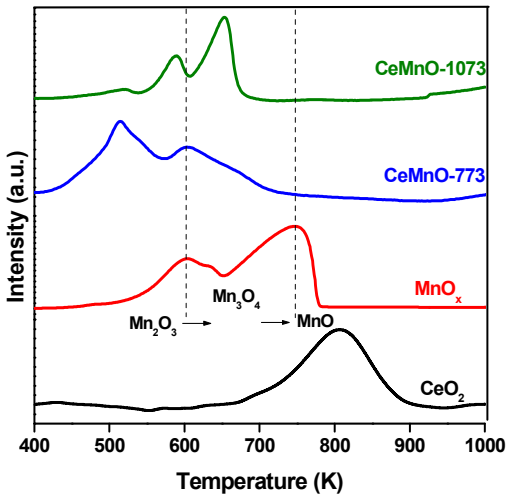

Fig. 5 H_2–TPR patterns of CeO_2 and MnO_x catalysts calcined at 773 K, and CeO_2–MnO_x catalysts calcined at 773 and 1073 K.

The O 1s spectra of pure CeO_2, CeMnO-773, and CeMnO-1073 samples are shown in Fig. 6B. The O 1s spectra of pure CeO_2 and MnO_x indicate the presence of both chemisorbed and lattice oxygen species on the catalyst surface. On the other hand, the O 1s spectra of CeO_2–MnO_x catalysts contained three types of oxygen species, in which the binding energy at ~529.1–530.2 eV was assigned to the lattice oxygen (O_I) while the binding energy

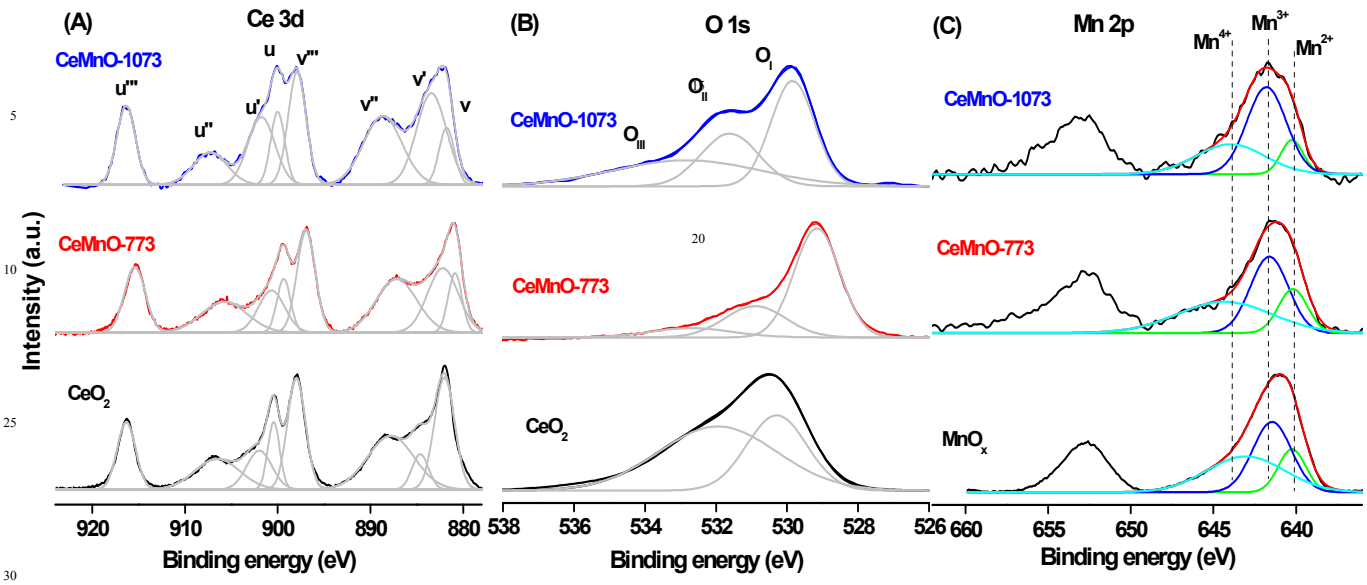

Fig. 6 (A) Ce 3d (B) O 1s (C) Mn 2p XP spectra of fresh CeO_2 and MnO_x catalysts calcined at 773K, and CeO_2–MnO_x catalysts calcined at 773 and 1073 K.

at ~530.6–531.9 eV was attributed to oxygen species in the defects or hydroxyl-like groups (denoted as O_{II}). Lastly, the binding energy at ~532.7–533.8 eV (O_{III}) can be attributed to carbonates/adsorbed water.[40] Interestingly, the binding energy of lattice oxygen (O_I) was decreased for CeMnO-773 sample while compared to pure CeO_2, which is evidenced from Table 2. It can be attributed to the O → Mn electron-transfer processes as the interactions between Ce and Mn are synergistic in nature where the dopant cation is having a decisive role towards the binding energy shift. As a result, the O → Mn in the CeO_2–MnO_x mixed oxide could enable the formation of very reactive electrophilic oxygen species (e.g., O^{2-}, O^-, $O^{\bullet}$).[43] It is well known that the defect oxygen species are responsible for oxidation reactions.[44] Therefore, the O_{II} species in the CeMnO-773 sample might be helpful for Hg^0 oxidation reaction.

In order to identify the oxidation states of Mn, the XPS spectra of Mn 2p was acquired and shown in Fig. 6C. It is clear that the co-existence of Mn^{2+}, Mn^{3+}, and Mn^{4+} species have been identified by the binding energies at ~640.2, 641.5, and 643.5 eV, respectively.[21,39,45] The observed binding energies of the manganese ions in the CeO_2–MnO_x samples are lower than pure MnO, MnO_2, and Mn_2O_3, which might be due to a strong interaction between manganese and cerium oxides.[30] As can be observed from Table 3, the CeMnO-773 sample showed more $Mn^{4+}/Mn^{3+}+Mn^{2+}$ ratio (1.15), while compared to pure MnO_x (0.63). It can be concluded that the combination of CeO_2 and MnO_x results in more surface Mn^{4+} concentration. Several authors reported that high valance having Mn oxides could enhance Hg^0 oxidation efficiency as the Mn^{4+} could directly oxidize the adsorbed Hg^0.[13,46] Further, they explained that the presence of Mn^{3+} also plays an important role in Hg^0 oxidation in the O_2 atmosphere. Therefore, the high ratio of $Mn^{4+}/Mn^{3+}+Mn^{2+}$ could be responsible for better Hg^0 oxidation.

3.2. Mercury oxidation

3.2.1 Effect of HCl, O_2, and HCl/O_2-mix

In coal derived flue gas streams, chlorine is believed to be present mainly as HCl. Therefore, it can be the most important species for effecting Hg^0 oxidation given that the product of oxidized Hg in coal combustion flue gas is largely found to be in the form of $HgCl_2$.[1] Fig. 7A shows the speciation of mercury in the presence of HCl over different catalysts calcined at 773 K. It can be observed that the amount of oxidised mercury was similar for all the investigated catalysts. Interestingly, the CeO_2–MnO_x mixed oxide and MnO_x catalysts showed more adsorbed mercury, 56.6 and 49.4 µg, respectively, when compared to pure ceria (28.5 µg). This was most likely due to the presence of more surface oxygen species of MnO_x and CeO_2–MnO_x catalysts. Additionally, the synergy between Ce and Mn in the CeO_2–MnO_x mixed oxide can be attributed to more adsorption ability over pure CeO_2 and MnO_x. The mercury capacities of CeO_2, MnO_x, and CeO_2–MnO_x in the presence of O_2 (about 3%) are shown in Fig. 7B. The presence of O_2 also resulted in less oxidised mercury, however the CeO_2–MnO_x catalyst showed reasonable oxidised mercury (20.5 µg) while compared to the oxidised mercury (7.2 µg) in the presence of HCl. Fig. 7C shows that when 3% O_2 and 10 ppm HCl were added to the reactor at the same time, the outlet Hg^0 value could drop to 0.02 µg, whereas the oxidised mercury value reached 54.9 µg, which was significantly higher than that in the case of adding O_2 or HCl separately. This result suggested that the presence of O_2 and HCl vapor together in simulated flue gas greatly promoted the Hg^0 oxidation.

3.2.2 Hg^0 vapor oxidation and adsorption performances of the catalysts

In order to ensure the validity of the oxidation and adsorption performances of the develop catalysts, we first determined the inlet Hg^0 concentration by running a series of 10 calibration experiments without the presence of any catalyst, the data of which is shown in Fig. S2 (ESI†). From the calibration graph, it is clear that the average inlet amount of Hg^0 is ~61.2 µg. Accordingly, the Hg^0 oxidation (E_{oxi}) and adsorption (E_{ads}) efficiencies over CeO_2, MnO_x, and CeO_2–MnO_x catalysts are shown in Fig. 8A and Fig. 8B, respectively. No obvious oxidation of Hg^0 was observed over pure CeO_2 and MnO_x. On the other hand, the CeO_2–MnO_x catalyst exhibited reasonable Hg^0 oxidation performance (11.7, and 33.5 % in presence of HCl and O_2, respectively) compared to pure CeO_2 and MnO_x. Additionally, the presence of 3% O_2 and 5% CO_2 and 10 ppm HCl gas mixture resulted in E_{oxi} of 89.6%, which was much higher than the E_{oxi} in the presence of either O_2 or HCl atmosphere alone. Clearly, the presence of HCl/O_2-mix has a promotional effect on Hg^0 oxidation. In contrast, the pure CeO_2 and MnO_x catalysts exhibited high adsorption efficiencies of 93.7 and 73.4 %, respectively. Therefore, it can be concluded that the pure metal oxides used in this study act as good Hg^0 vapor adsorbents, whereas the CeO_2–MnO_x mixed oxide catalyst has superior catalytic properties. However, the CeO_2–MnO_x catalyst was found to have higher Hg content adsorbed on the surface when HCl only was present in the gas mixture. To study this phenomenon further, the catalytic oxidation and adsorption behaviour of CeO_2–MnO_x catalyst towards Hg^0 in presence of HCl at various different temperatures was studied, the results of which are shown in Fig. 9. It can be observed that as the temperature increases from 423 to 523 K, the oxidation efficiency also increased from 11.7 to 80 %, however the efficiency decreases when the temperature is further increased to 573 K. It can be concluded that increased operating temperature promotes Hg^0 oxidation efficiency up to a certain temperature. Thereafter, the significant desorption of adsorbed Hg^0 at higher temperatures might inhibit oxidation and adsorption efficincies.[10] Based on the observed scenario, the plausible reaction path may be a heterogeneous oxidation (through the Langmuir-Hinshelwood mechanism) of Hg^0 on the CeO_2–MnO_x catalyst when O_2 and HCl are present. Several authors have previously indicated that the oxygen vacancies play an important role in the catalytic activity due to the formation of intermediate species like superoxide (O^{2-}) ions in the oxidative reactions, which are accruing on the catalysts surface.[25,47,48] In the current study, it was found that the CeO_2–MnO_x catalyst is more active in terms of redox behaviour than the pure CeO_2 or MnO_x (Fig. 5), which can also be possibly related to a higher concentration of surface oxygen vacancies (Fig. 4) due to the partial replacement of Ce^{4+} by Mn^{x+} in the CeO_2 lattice. Accordingly, the oxygen vacancies provide sites for oxygen activation to form superoxide (O^{2-}) species. At the same time, HCl adsorbed on the CeO_2–MnO_x catalyst surface was first oxidized to active Cl species. Then the active Cl (Cl*) would react with adjacent adsorbed Hg^0 to produce $HgCl_2$, thus leaving empty oxygen vacancies and closing the catalytic cycle.[49] Additionally, the higher E_{oxi} for CeO_2–MnO_x catalyst can be attributed to the effect of multiple oxidation states (+4, +3, and +2) of Mn on the redox ability of $Ce^{4+} \leftrightarrow Ce^{3+}$, which is confirmed from Raman, H_2-TPR, and XPS observations.

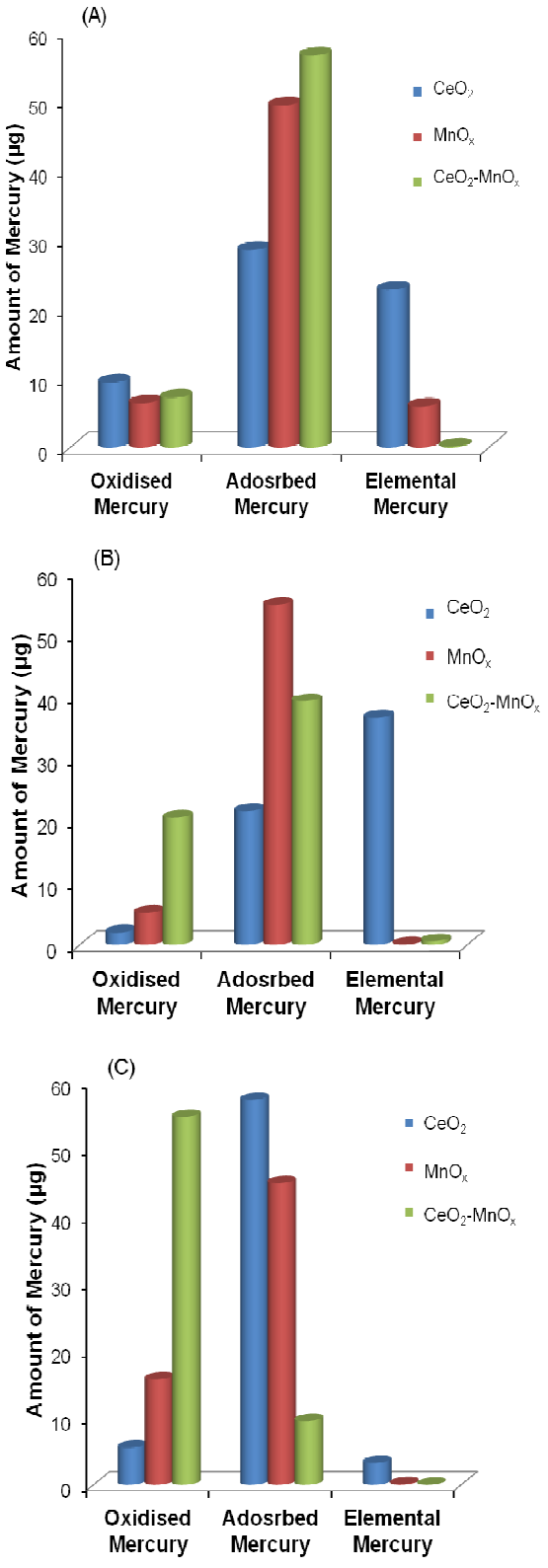

Fig. 7 Hg speciation over CeO_2, MnO_x, and CeO_2–MnO_x catalysts calcined at 773 K under different flue gas conditions (A) HCl (B) O_2 (C) HCl and O_2.

The effect of cerium to the catalysis might be attributed to its promotion on the cycle between Mn^{3+} and Mn^{4+}, which would speed up the transfer of oxygen and the formation of active chlorine species. Therefore, it can be concluded that the combination of Ce and Mn in the catalyst matrix had an obvious accelerative effect on Hg^0 removal relative to their individual respective oxides.

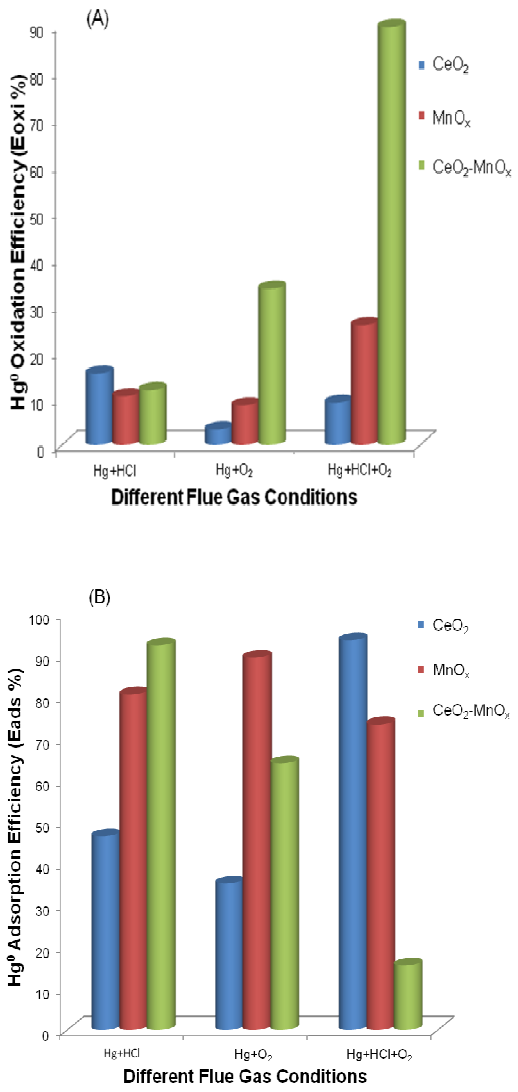

Fig. 8 (A) Hg^0 oxidation (E_{oxi}) and (B) Hg^0 adsorption (E_{ads}) efficiencies of CeO_2, MnO_x, and CeO_2–MnO_x catalysts calcined at 773 K under different flue gas conditions

$$2HCl_{(g)} + O^* \rightarrow 2Cl^*_{(ad)} + H_2O \quad (4)$$

$$Hg^0_{(g)} \rightarrow Hg^0_{(ad)} \quad (5)$$

$$Cl^*_{(ad)} + Hg^0_{(ad)} \rightarrow HgCl^*_{(ad)} \quad (6)$$

$$HgCl^*_{(ad)} + Cl^*_{(ad)} \rightarrow HgCl_{2(ad)} \quad (7)$$

$$HgCl_{2(ad)} \rightarrow HgCl_{2(g)} \quad (8)$$

In this reaction, O* represents chemisorbed or lattice oxygen on the surface of CeO_2–MnO_x catalyst, which can be consumed by HCl. During the reaction, an intermediate product (HgCl*) is formed which subsequently oxidized by other active chlorine species to form $HgCl_2$.[50]

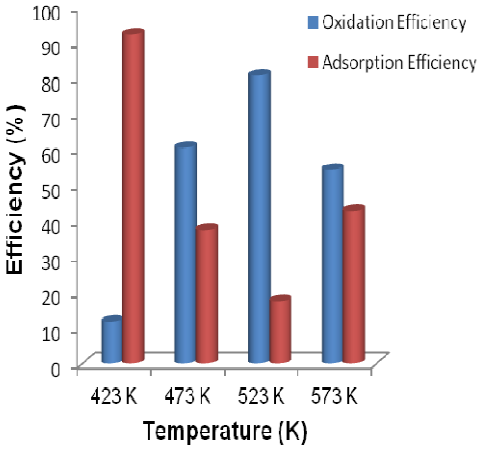

Fig. 9 Hg^0 oxidation (E_{oxi}) and adsorption (E_{ads}) efficiencies of CeO_2–MnO_x catalysts calcined at 773 K in presence of HCl under different temperatures from 423 to 573 K.

Furthermore, to obtain more insight into the interaction between CeO_2 and MnO_x in the mixed oxide due to mercury adsorption in the presence of HCl and O_2, XPS measurements were conducted on the spent catalysts. The Ce 3d, O 1s, and Mn 2p XP spectra of used CeO_2, MnO_x, and CeO_2–MnO_x catalysts were shown in Fig. S3A, Fig. S3B, and Fig. S3C (ESI†), respectively. After Hg^0 saturation adsorption at 423 K, the intensity of Ce^{4+} peaks in Ce 3d spectra decreased, which indicates a reduction of Ce^{4+} during Hg^0 oxidation. For CeMnO-773 sample, the ratio of Ce^{4+}/Ce^{3+} decreased from 3.14 to 1.36 (Table 3) after mercury oxidation and adsorption experiments. It can be due to the easily generated labile oxygen vacancies and high mobile oxygen during the redox process of $Ce^{4+} \leftrightarrow Ce^{3+}$. In addition, this observation revealed the possibility of the reaction between cation vacancies and Hg^0 during the oxidation process. As observed from Table 2 and Table S2 (ESI†), the significant shift of Ce 3d level of the used CeO_2 catalyst to the lower energy side compared to CeO_2–MnO_x mixed oxide confirms the strongly electro-negative chlorine species adsorbed on CeO_2 sites. On the other hand, the binding energy shifts of CeO_2–MnO_x are slight, due to a weak adsorption of chlorine species. Therefore, the combination of CeO_2 with MnO_x decreased adsorption efficiency and increased oxidation efficiency. The intensity decrease of Mn 2p peaks in the used CeO_2–MnO_x catalyst was due to the adsorption of mercury species on the surface. Particularly, the ratio decrease of $Mn^{4+}/Mn^{3+}+Mn^{2+}$ confirms the occurrence of the reaction between the active species and lattice oxygen provided by MnO_x. Therefore, it could be concluded that the presence of the active Ce^{4+} and Mn^{4+} phases as well as the formation of Ce^{3+} (or oxygen

vacancies) contributed to high catalytic activity, which are strongly supported by XPS results. The Hg 4f and Cl 2p spectra of all of the MnO_x, CeO_2, and CeO_2–MnO_x catalysts were also shown in Fig. S4A and Fig. S4B (ESI†), respectively. The peak at lower binding energy could be due to elemental mercury, and the peak at higher binding energy is due to either HgO or $HgCl_2$. For MnO_x sample, the binding energies of Hg $4f_{7/2}$ at 101.3 eV and Hg $4f_{5/2}$ at 103.0 eV correspond to the oxidized mercury (HgO).[51] On the other hand, the peak due to the HgO or $HgCl_2$ is larger for CeO_2–MnO_x mixed oxide compared to the other samples. It is clear that the oxidised mercury can be in the form of HgO/$HgCl_2$. Additionally, the Cl 2p peak appearing at ~198 eV confirm the presence of chlorine species in the form of $HgCl_2$ on all of the used catalysts.

Table 3 The surface atomic ratios of fresh and spent catalysts calcined at 773 K.

Catalyst	Ce^{4+}/Ce^{3+}		$Mn^{4+}/Mn^{3+}+Mn^{2+}$	
	fresh	spent	fresh	spent
MnO_x	-	-	0.63	0.25
CeO_2	5.04	4.87	-	-
CeMnO-773	3.14	1.36	1.15	0.46

4. Conclusions

The nanostructured CeO_2–MnO_x catalyst was successfully prepared by a coprecipitation method from cerium and manganese nitrate precursors. The physicochemical properties were deeply investigated by various state of the art techniques. The XRD and TEM results confirmed the formation of nanosized $Ce_{0.7}Mn_{0.3}O_{2-\delta}$ solid solutions with a cubic phase of fluorite structure. The Raman results revealed the presence of more oxygen vacancies in the CeO_2–MnO_x mixed oxide compared to pure metal oxides. H_2-TPR measurements show that there was a synergetic effect between CeO_2 and MnO_x in the mixed oxide. XPS results of fresh and spent catalysts suggested that Ce^{4+} and Mn^{4+} species contributed to more Hg^0 oxidation performance. Among all the investigated catalysts, the CeO_2–MnO_x mixed oxide exhibited superior activity toward Hg^0 oxidation compared to pure CeO_2 or MnO_x. The better activity could be attributed to the formation of more oxygen vacancies and facile redox behavior, which is resulted owing to strong synergetic effect between CeO_2 and MnO_x. The effects of various other flue gas constituents such as NO_x, NH_3, SO_2, and water vapor on Hg^0 oxidation efficiency of the developed CeO_2–MnO_x catalyst is the subject of future work.

Acknowledgements

D. J. thanks the RMIT-IICT Joint Research Center for providing the Junior Research Fellowship.

†Electronic supplementary information (ESI) available: the chemical compositions of CeO_2–MnO_x mixed oxides, binding energies of spent catalysts, experimental diagram, calibration experiments for Hg^0_{inlet}, Ce 3d, O 1s, Mn 2p, Hg 4f and Cl 2p XPS spectra of spent catalysts calcined at 773 K.

References

1 J. Zhou, W. Hou, P. Qi, X. Gao, Z. Luo and K. Cen, *Environ. Sci. Technol.,* 2013, **47**, 10056–10062.
2 B. M. Reddy, N. Durgasri, T. V. Kumar and S. K. Bhargava, *Catal. Rev. - Sci. Eng.,* 2012, **54**, 344–398.
3 C. Sun, C. E. Snape and H. Liu, *Energy Fuels*, 2013, **27**, 3875–3882.
4 D. Jampaiah, K. M. Tur, S. J. Ippolito, Y. M. Sabri, J. Tardio, S. K. Bhargava and B. M. Reddy, *RSC Adv.,* 2013, **3**, 12963–12974.
5 A. A. Presto, E. J. Granite, A. Karash, R. A. Hargis, W. J. O'Dow and H. W. Pennline, *Energy Fuels*, 2006, **20**, 1941–1945.
6. S. Yang, Y. Guo, N. Yan, Z. Qu, J. Xie, C. Yang and J. Jia, *J. Hazard. Mater.,* 2011, **186**, 508–515.
7. A. P. Jones, J. W. Hoffmann, D. N. Smith, T. J. Feeley and J. T. Murphy, *Environ. Sci. Technol.,* 2007, **41**, 1365–1371.
8 A. A. Presto and E. J. Granite, *Environ. Sci. Technol.,* 2007, **41**, 6579–6584.
9 G. Luo, H. Yao, M. Xu, X. Cui, W. Chen, R. Gupta and Z. Xu, *Energy Fuels*, 2009, **24**, 419–426.
10 Y. M. Sabri, S. J. Ippolito and S. K. Bhargava, *J. Phys. Chem. C*, 2013, **117**, 8269–8275.
11 A. A. Presto and E. J. Granite, *Environ. Sci. Technol.,* 2006, **40**, 5601–5609.
12 K. S. Park, Y. C. Seo, S. J. Lee and J. H. Lee, *Powder Technol.*, 2008, **180**, 151–156.
13 P. Wang, S. Su, J. Xiang, F. Cao, L. Sun, S. Hu and S. Lei, *Chem. Eng. J.,* 2013, **225**, 68–75.
14 J.-r. Li, C. He, X.-s. Shang, J.-s. Chen, X.-w. Yu and Y.-j. Yao, *J. Fuel Chem. Technol.,* 2012, **40**, 241–246.
15 P. Venkataswamy, K. N. Rao, D. Jampaiah and B. M. Reddy, *Appl. Catal., B,* 2015, **162**, 122–132.
16 Y. Gao, Z. Zhang, J. Wu, L. Duan, A. Umar, L. Sun, Z. Guo and Q. Wang, *Environ. Sci. Technol.,* 2013, **47**, 10813–10823.
17 H. Kamata, S.-i. Ueno, T. Naito, A. Yamaguchi and S. Ito, *Catal. Commun.,* 2008, **9**, 2441–2444.
18 Y. Liu, Y. Wang, H. Wang and Z. Wu, *Catal. Commun.,* 2011, **12**, 1291–1294.
19 Z. Chen, Z. Jiao, D. Pan, Z. Li, M. Wu, C.-H. Shek, C. M. L. Wu and J. K. L. Lai, *Chem. Rev.*, 2012, **112**, 3833–3855.
20 C. He, B. Shen, J. Chen and J. Cai, *Environ. Sci. Technol.,* 2014, **48**, 7891–7898.
21 L. Ji, P. M. Sreekanth, P. G. Smirniotis, S. W. Thiel and N. G. Pinto, *Energy Fuels*, 2008, **22**, 2299–2306.
22 Q. Wan, L. Duan, K. He and J. Li, *Chem. Eng. J.,* 2011, **170**, 512–517.
23 J. Li, N. Yan, Z. Qu, S. Qiao, S. Yang, Y. Guo, P. Liu and J. Jia, *Environ. Sci. Technol.,* 2009, **44**, 426–431.
24 Y. Guo, N. Yan, S. Yang, P. Liu, J. Wang, Z. Qu and J. Jia, *J. Hazard. Mater.,* 2012, **213–214**, 62–70.
25 H. Li, C.-Y. Wu, Y. Li and J. Zhang, *Appl. Catal., B*, 2012, **111–112**, 381–388.
26 P. Wang, S. Su, J. Xiang, H. You, F. Cao, L. Sun, S. Hu and

Y. Zhang, *Chemosphere*, 2014, **101**, 49–54.
27 J. Q. Sun, K. S. Uhrich and R. L. Schulz, *Prepr. Pap.-Am. Chem. Soc., Div. Fuel Chem.,* 2003, **48**, 774–776.
28 B. C. Sekhar, G. Babu and N. Kalaiselvi, *RSC Adv.*, 2015, **5**, 4568–4577.
29 K. N. Rao, P. Bharali, G. Thrimurthulu and B. M. Reddy, *Catal. Commun.,* 2010, **11**, 863–866.
30 W.-J. Hong, S. Iwamoto, S. Hosokawa, K. Wada, H. Kanai and M. Inoue, *J. Catal.,* 2011, **277**, 208–216.
31 Z.-Q. Zou, M. Meng and Y.-Q. Zha, *J. Phys. Chem. C*, 2009, **114**, 468–477.
32 H. Li, Tana, X. Zhang, X. Huang and W. Shen, *Catal. Commun.*, 2011, **12**, 1361–1365.
33 Z. Yang, Y. Zhang, W. Zhang, X. Wang, Y. Qian, X. Wen and S. Yang, *J. Solid State Chem.,* 2006, **179**, 679–684.
34 X. Li, X. Lu, Y. Meng, C. Yao and Z. Chen, *J. Alloys Compd.*, 2013, **562**, 56–63.
35 F. d. A. A. Barros, H. S. A. de Sousa, A. C. Oliveira, M. C. Junior, J. M. Filho, B. C. Viana and A. C. Oliveira, *Catal. Today*, 2013, **212**, 127–136.
36 F. Buciuman, F. Patcas, R. Craciun and D. R. T. Zahn, *Phys. Chem. Chem. Phys*., 1999, **1**, 185–190.
37 L. Katta, G. Thrimurthulu, B. M. Reddy, M. Muhler and W. Grunert, *Catal. Sci. Technol.,* 2011, **1**, 1645–1652.
38 A. Gupta, U. V. Waghmare and M. S. Hegde, *Chem. Mater*., 2010, **22**, 5184–5198.
39 L. Qu, C. Li, G. Zeng, M. Zhang, M. Fu, J. Ma, F. Zhan and D. Luo, *Chem. Eng. J.,* 2014, **242**, 76–85.
40 P. Zhao, C. Wang, F. He and S. Liu, *RSC Adv.*, 2014, **4**, 45665–45672.
41 H. Zhang, F. Gu, Q. Liu, J. Gao, L. Jia, T. Zhu, Y. Chen, Z. Zhong and F. Su, *RSC Adv.*, 2014, **4**, 14879–14889.
42 Z.-Q. Zou, M. Meng and Y.-Q. Zha, *J. Phys. Chem. C*, 2009, **114**, 468–477.
43 W. Xingyi, K. Qian and L. Dao, *Appl. Catal., B*, 2009, **86**, 166–175.
44 F. Arena, G. Trunfio, J. Negro, B. Fazio and L. Spadaro, *Chem. Mater.,* 2007, **19**, 2269–2276.
45 R. Xu, X. Wang, D. Wang, K. Zhou and Y. Li, *J. Catal.*, 2006, **237**, 426–430.
46 J. Xie, Z. Qu, N. Yan, S. Yang, W. Chen, L. Hu, W. Huang and P. Liu, *J. Hazard. Mater.*, 2013, **261**, 206–213.
47 C. Bozo, N. Guilhaume and J.-M. Herrmann, *J. Catal.,* 2001, **203**, 393–406.
48 Z.-Y. Pu, X.-S. Liu, A.-P. Jia, Y.-L. Xie, J.-Q. Lu and M.-F. Luo, *J. Phys. Chem. C*, 2008, **112**, 15045–15051.
49 P. Wang, S. Su, J. Xiang, H. You, F. Cao, L. Sun, S. Hu and Y. Zhang, *Chemosphere*, 2014, **101**, 49–54.
50 H. Kamata, S.-i. Ueno, N. Sato and T. Naito, *Fuel Process. Technol.*, 2009, **90**, 947–951.
51 J. He, G. K. Reddy, S. W. Thiel, P. G. Smirniotis and N. G. Pinto, *J. Phys. Chem. C,* 2011, **115**, 24300–24309.